Revealing the Formation of Copper Nanoparticles from a Homogeneous Solid Precursor by Electron Microscopy

Roy van den Berg,[†] Christian F. Elkjaer,[‡,§] Cedric J. Gommes,[‖] Ib Chorkendorff,[§] Jens Sehested,[‡] Petra E. de Jongh,[†] Krijn P. de Jong,[†] and Stig Helveg*,[‡]

[†]Inorganic Chemistry and Catalysis, Debye Institute for Nanomaterials Science, Utrecht University, Universiteitsweg 99, 3584 CG Utrecht, Netherlands

[‡]Haldor Topsoe A/S, Haldor Topsøes Allé 1, DK-2800 Kgs. Lyngby, Denmark

[§]Department of Physics, Technical University of Denmark, Fysikvej 312, DK-2800 Kgs. Lyngby, Denmark

[‖]Department of Chemical Engineering, University of Liège, Allée du 6 août 3, B-4000 Liège, Belgium

S *Supporting Information*

ABSTRACT: The understanding of processes leading to the formation of nanometer-sized particles is important for tailoring of their size, shape and location. The growth mechanisms and kinetics of nanoparticles from solid precursors are, however, often poorly described. Here we employ transmission electron microscopy (TEM) to examine the formation of copper nanoparticles on a silica support during the reduction by H_2 of homogeneous copper phyllosilicate platelets, as a prototype precursor for a coprecipitated catalyst. Specifically, time-lapsed TEM image series acquired of the material during the reduction

process provide a direct visualization of the growth dynamics of an ensemble of individual nanoparticles and enable a quantitative evaluation of the nucleation and growth of the nanoparticles. This quantitative information is compared with kinetic models and found to be best described by a nucleation-and-growth scenario involving autocatalytic reduction of the copper phyllosilicate followed by diffusion-limited or reaction-limited growth of the copper nanoparticles. The plate-like structure of the precursor restricted the diffusion of copper and the autocatalytic reduction limited the probability for secondary nucleation. The combination of a uniform size of precursor particles and the autocatalytic reduction thus offers means to synthesize nanoparticles with well-defined sizes in large amounts. In this way, in situ observations made by electron microscopy provide mechanistic and kinetic insights into the formation of supported nanoparticles, essential for the rational design of nanomaterials.
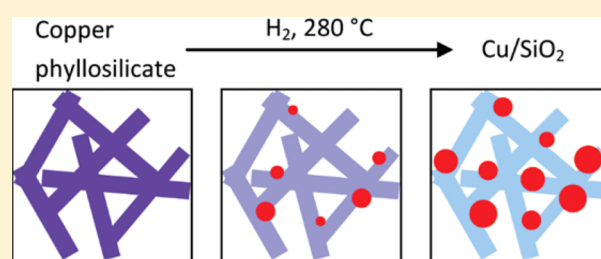
◼ INTRODUCTION

Nanometer-sized particles provide electronic, optical and catalytic properties that strongly depend on their size, shape and spatial arrangement. The synthesis of nanoparticles with predefined structural characteristics has therefore become an important research theme. Synthesis procedures include the aggregation of atomic species to form colloidal nanoparticles in liquid phase and the transformation of solid precursors by gas phase treatments to form supported nanoparticles.[1] In the latter case, precursors often consist of a metal salt impregnated on a solid support or of a coprecipitate of the metal oxide and support material. This approach is particularly beneficial for preparing nanoparticles at large scales for, e.g., industrial catalytic processes.[1a−c] Despite the significant efforts devoted to optimize procedures for transforming solid precursors into supported nanoparticles, a fundamental understanding of the particle growth mechanisms and their relation with the growth kinetics is often limited.[2] As growth processes involve atom exchange at or across solid surfaces, observations made in situ at high-spatial resolution would be beneficial for elucidating nanoparticle growth mechanisms.

In recent years, transmission electron microscopy (TEM) has become a powerful tool for visualizing nanoparticles at atomic-resolution.[3] Studies of nanomaterials during exposure to gas or liquid environments are, however, hampered by the small mean free path of the electron beam in dense media. The introduction of differentially pumped vacuum systems and closed electron-transparent cells provides a means to confine gas or liquid phases to the vicinity of the sample in transmission electron microscopes.[4] Hereby, TEM can be used to monitor nanomaterials in reactive environments by the acquisition of time-lapsed image series. This approach has resulted in new insights into the formation of nanoparticles in the liquid phase,[5] and, by gas phase treatment of impregnated support materials, in the solid phase.[6] However, the way in which nanoparticles grow in the solid phase by gas phase treatment of coprecipitated precursors has not been addressed so far, although homogeneity of these materials offers the possibility

to obtain mechanistic and kinetic information that can be translated to large-scale material synthesis.

Here we use TEM to examine the growth of an ensemble of Cu nanoparticles on SiO_2, which represents a material that catalyzes the hydrogenation of carbon–oxygen bonds.[7] The nanoparticles and the silica support are formed in the electron microscope by reduction in H_2 of copper phyllosilicate, which is a precipitated solid precursor that consists of platelets with a homogeneous distribution of Cu^{2+}.[8] To ensure that the TEM observations reflect processes inherent to the reduction treatment, the impact of the electron beam on the process was characterized and a beam-insensitive imaging scheme was developed. By employing this optimized imaging scheme, time-resolved TEM images were acquired during the formation of the copper nanoparticles which enabled the extraction of quantitative information about the nucleation and growth of individual copper nanoparticles. This dynamic information is compared to predictions made by kinetic models which allowed deriving a mechanism for the nanoparticle formation.

■ EXPERIMENTAL SECTION

Synthesis of Copper Phyllosilicate. Copper phyllosilicate can be synthesized by deposition precipitation of copper nitrate using ammonia evaporation[7a,d,9] or urea hydrolysis[8b] and by using selective adsorption of $[Cu(NH_3)_4]^{2+}$ on SiO_2.[8a] Both deposition-precipitation and selective adsorption often lead to heterogeneous materials comprising unreacted silica, copper phyllosilicate, and other copper species like copper(II) oxide.[8] To obtain only the copper phyllosilicate phase, the homogeneous deposition-precipitation procedure of van der Grift and co-workers[8b] was followed including a hydrothermal treatment.

Specifically, a mass of 20.1 g of LUDOX-AS 30 (Sigma-Aldrich), 16.1 g of $Cu(NO_3)_2 \cdot 3H_2O$ (Acros Organics, 99% for analysis) and 12.1 g of Urea (Acros Organics, 99.5% for analysis) were added to 1.7 L of demineralized water in a 2 L reaction vessel. The pH was adjusted to 2–3 with a few drops of HNO_3 (Merck, 65% for analysis) to prevent premature hydrolysis of copper nitrate. The suspension was then heated to 90 °C in 1 h under stirring. At 90 °C, hydrolysis of urea led to an increase in pH resulting in the precipitation of $Cu_2(NO_3)(OH)_3$ and the formation of the $[Cu(OH)_2(H_2O)_4]^0$ complex in solution. The well-stirred suspension was kept at 90 °C for 7 days to allow recrystallization of precipitated copper and silica, which resulted in the formation of copper phyllosilicate. The precipitate was obtained by hot filtration of the suspension. Thereafter, the precipitate was washed three times at room temperature with demineralized water, filtered and dried overnight at 60 °C. The yield was about 10 g, which is close to the intended dry copper phyllosilicate weight. A relatively high copper to silicon atomic ratio of 0.66 was chosen, corresponding to 41 wt % copper in the final Cu/SiO_2 material. Lower copper loadings resulted in partly unreacted silica and a copper loading above 45 wt % resulted in the presence of copper oxide particles.[7b]

Reduction in a Plug-Flow Reactor. A mass of 0.3 g of the as-prepared copper phyllosilicate was reduced in a plug-flow reactor (diameter 1 cm) at 250 °C (heating rate 2 °C/min) in a flow of 30 mL/min of 20% H_2 in Ar for 2 1/2 h. After the reduction treatment, the reduced sample was passivated for 15 min at room temperature by slowly exposing the sample to a diluted air/N_2 flow by creating a small leak in the flow supply system. The sample was stored in a glovebox containing an argon atmosphere.

Characterization. X-ray diffraction was performed with a Bruker-Nonius D8 Advance X-ray diffractometer using Co–$K_{\alpha1,2}$ (λ = 1.79026 Å) radiation. For the reduced sample, the specimen holder was loaded in the glovebox and subsequently sealed to prevent exposure to air. Diffractograms of the material before and after reduction were obtained at room temperature from 20° to 70° (2θ). N_2 physisorption measurements were performed at −196 °C, using a

Micromeritics Tristar 3000 apparatus. The BET method was used to calculate the specific surface area. Energy dispersive X-ray (EDX) spectroscopy was performed using a Technai 20FEG (FEI) electron microscope equipped with a field emission gun and with an EDAX Super Ultrathin Window EDX detector. The as-prepared copper phyllosilicate was dispersed on a carbon-coated Ni grid (Agar 162 200 Mesh Ni) and this sample was introduced into the microscope using a low-background sample holder (Philips) with a 0.1 mm thick Be specimen support film and a Be ring to clamp the grid. EDX spectra were acquired during scanning transmission electron microscopy (STEM) with a 0.3−1.2 nm wide electron beam of 22 different square regions extending from 100 nm to 1 μm in width and of 6 different lines of 100 to 500 nm in length. The EDX spectra were quantified using the Tecnai Imaging and Analysis (TIA) software by using a detector correction of 0.977 and 0.997 and a k-factor of 1.000 and 1.757 for Si and Cu, respectively, in converting the integrated intensities of the Si K and Cu K peaks, subsequent to a manual background correction, to element concentrations. Temperature-programmed reduction (TPR) was performed using an Autochem II ASAP 2910 from Micromeritics. The H_2 concentration during the experiment was measured with a thermal conductivity detector. About 0.05 g copper phyllosilicate was placed on top of a quartz wool bed in a glass reactor tube. The sample was heated to 500 °C (5 °C/min) under a flow of 5% H_2/Ar. Thermal gravimetric analysis (TGA) was performed with a PerkinElmer Pyris 1 apparatus. About 2.5 mg of copper phyllosilicate was heated to 500 °C under a flow of 2.5 mL/min 5% H_2/Ar.

Transmission Electron Microscopy. In situ observations by TEM were made using an image-aberration corrected Titan 80−300 ETEM (FEI Company).[10] The microscope was operated at a primary electron energy of 300 keV. Prior to an experiment, the image-aberration corrector was tuned using a cross-grating (Agar S106) and the spherical aberration coefficient was set in the range of −10 to −20 μm. All quoted electron dose-rates were measured using the microscope's fluorescent screen. TEM grids were placed in a heating holder (Gatan model 628) for introduction into the electron microscope and subsequent heating of the sample. TEM images were acquired with a bottom-mounted 2k × 2k charged-coupled device (CCD) camera (Gatan US1000) and with the projection system set to an effective CCD pixel size between 0.37 and 0.56 nm.

The reduced Cu/SiO_2 was used as reference. A sample was prepared by grinding the powder and dispersing it on a stainless steel grid. The sample was exposed to 1 mbar H_2 at 250 °C (heating rate 30 °C/min) for 45 min to rereduce the copper that was oxidized during the passivation treatment. Under these conditions, TEM images of the sample were acquired using an electron dose-rate of 10 and 100 e^-/($Å^2$ s).

The as-prepared copper phyllosilicate was studied in different types of experiments in the electron microscope to address the effect of temperature and the effect of electron illumination, including the electron dose-rate, accumulated, dose, and illumination history, on the formation of copper particles. Specifically, the first experiment addressed the effect of thermal reduction in H_2 without any electron beam illumination. Herein, separate samples were exposed to 1 mbar H_2 at 150 °C (4 h), 200 °C (1/2 h), 250 °C (3 h) and 280 °C (1 1/4 h) and subsequently imaged at the respective conditions or at base vacuum (1.9 × 10^{-6} mbar) at room temperature. Two additional experiments addressed the effect of electron illumination of the sample in vacuum prior to a reduction treatment, and the effect of the electron illumination in H_2 with no thermally induced particle growth (see section Electron-beam induced changes in the Supporting Information). The results of these experiments made it possible to establish an experimental procedure to image the process of particle formation (Figure 1) for which beam-induced dynamics are suppressed and temporal and spatial resolution are optimized.

Following the procedure in Figure 1, time-resolved TEM observations were obtained of two samples, which were prepared by grinding and dispersing the as-prepared copper phyllosilicate on gold grids. In the microscope, the samples were exposed to 1 mbar H_2 and heated at 30 °C/min to 200 °C. At these conditions, regions of
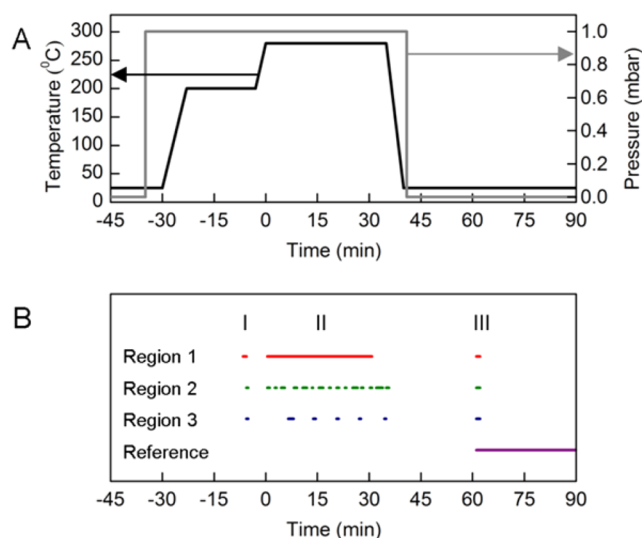
Figure 1. Procedure for TEM image acquisition during H_2 reduction of the copper phyllosilicate. (A) Temporal profiles of temperature and H_2 pressure in the experiment. Time $t = 0$ min corresponds to the time at which the temperature reaches 280 °C. (B) Scheme for electron illumination. The electron dose-rate: 0.05 $e^-/(Å^2 \text{ s})$ (before reduction (I)), 1 $e^-/(Å^2 \text{ s})$ (during reduction (II)) and 5 $e^-/(Å^2 \text{ s})$ (after reduction (III)). During reduction, Region 1 (red) was continuously illuminated and Region 2 (green) and Region 3 (blue) were intermittently illuminated at time intervals of ca. 2 and 6 min, respectively. After reduction, TEM images were acquired of regions 1–3 and at previously unilluminated regions (purple).

interest were identified with an electron dose-rate of 0.05 $e^-/(Å^2 \text{ s})$ and maximum illumination time of 1 min per region. After 20 min, thermal drift of the heating holder subsided and the samples were further heated to 280 °C (heating rate 30 °C/min). At those conditions, time-lapsed TEM images were recorded with an electron dose-rate of 1 $e^-/(Å^2 \text{ s})$. Specifically, by operating the projection system corresponding to a CCD camera pixel size of 0.56 nm and a CCD illumination time of 1 s, the electron beam penetrating only the gas phase creates on average about 32 electrons per pixel with a standard deviation of about 8 electrons, resulting in a signal-to-noise ratio (SNR) of 4. Because of this low SNR, particles were only distinguishable in the present phyllosilicate materials at diameters larger than ca. 3.4 nm (6 pixels). In comparison, the sample after full reduction in the microscope was examined by TEM at illumination conditions corresponding to an image SNR of about 20, and the sample reduced in the plug-flow reactor was examined by TEM with an image SNR of about 25. Both samples showed similar particle size distributions and a lower cutoff particle size of ca. 3 nm. Hence, the illumination conditions employed during the reduction process were sufficient to monitor the growth of all the particles.

The time-lapsed images were acquired as outlined in the scheme in Figure 1: In one experiment, one region (Region 1) was continuously illuminated and images acquired with a CCD illumination time of 1 s and a frame rate of 1 per 5 s. In a second experiment, two distinct regions (Region 2 and Region 3), outside of each other's illuminated areas, were illuminated at intervals of ca. 2 and 6 min, respectively. The illumination persisted for approximately 45 s, for locating and focusing the sample region and for subsequent image acquisition by illuminating the CCD for 2 s. Figure 1B denotes the exact times for electron illumination of each region. In the intervening periods between successive electron illuminations, the electron beam was blanked off or moved to the other location. With this illumination scheme, the accumulated electron dose for Region 1, 2, and 3 was 1735, 620, and 230 $e^-/Å^2$, respectively. After 30 min at 1 mbar H_2 at 280 °C, the sample was cooled to room temperature and the microscope was evacuated to its base vacuum (1.9×10^{-6} mbar). Under those conditions, TEM images were acquired of Region 1–3 as

well as reference areas on the two samples at 5 $e^-/(Å^2 \text{ s})$, which did not lead to any detectable changes to the sample.

Image Analysis. The time-resolved TEM image series provide information about the time for the first visual appearance of the copper particles and about the subsequent evolution of the copper particle size. For the different experiments, this information is evaluated by selecting 20 or 25 visually distinguishable particles in the last image of a time-series of images. The individual particles were tracked backward in time in the earlier acquired images until the image of their first visual appearance. This tracking was possible because all of the particles remained immobile. In each image, the particle diameter (referred to as size) is determined by measuring the projected area manually with ImageJ and by using a circular approximation to the measured area. Particle size distributions (PSDs) were obtained to compare the size of the copper particles after the different experiments. PSDs can appear visually distinct while others can appear similar. To provide a quantitative assessment of the similarity of PSDs that considers the statistical significance of the limited number of particles included in the analysis, the ANOVA method was used to determine the probability that two different PSDs had the same mean particle size.[11] With this method, the PSDs were considered significantly different, if the probability was lower than 2.5% ($p_{(\text{same mean size})} < 0.025$). To evaluate the progress of the particle formation, the evolution of the particle size should be combined with the evolution of the particle density. A simplistic measure, the "stage of particle evolution", quantifies the size and density evolution in a combined way by considering at each time the average size of the same 20 or 25 copper particles, including the particle size of 0 nm for particles prior to their first appearance.

■ RESULTS AND DISCUSSION

Copper Phyllosilicate. The composition and structure of the as-prepared copper phyllosilicate was examined by several experimental techniques. X-ray diffraction shows that the as-prepared copper phyllosilicate mainly consisted of an amorphous phase (Figure 2A, blue), in agreement with earlier
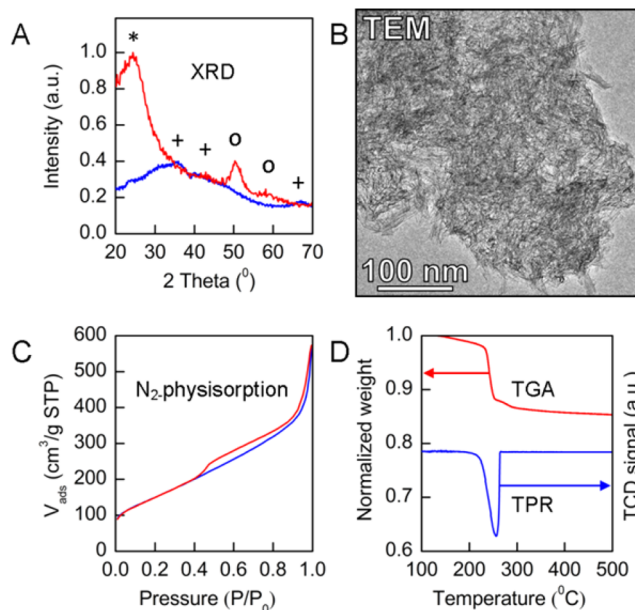

Figure 2. Characterization of the copper phyllosilicate. (A) X-ray diffractograms of the material before (blue) and after (red) reduction in the plug-flow reactor. The peak positions correspond to chrysocolla (+), silica (*) and metallic copper (○). (B) A TEM image of the as-prepared copper phyllosilicate. (C) N_2 physisorption of the as-prepared copper phyllosilicate (adsorption blue, desorption red). (D) TPR (blue) and TGA (red) of copper phyllosilicate in H_2/Ar flow.

observations.[8a] Weak diffraction peaks reveal a minor crystalline phase corresponding to chrysocolla ($Cu_2Si_2O_5(OH)_2 \cdot nH_2O$), which is a form of copper phyllosilicate.[8] Diffraction peaks characteristic for silica or other copper species were absent. The reaction between copper and silica was furthermore confirmed by the BET surface area, which increased from 100 m^2/g for colloidal silica to 550 m^2/g for the as-prepared copper phyllosilicate, in agreement with a previous report.[8b] Moreover, TEM images as in Figure 2B reveal that the material consisted of platelets with a width and thickness in the range of 5 to 20 nm and a length of up to 100 nm. The anisotropic morphology was confirmed by a N_2 physisorption profile that is typical for aggregates of platelets (Figure 2C).[8b,9] The TEM images did not show any particles with a spherical morphology as the original colloidal silica spheres and therefore also indicate a complete reaction with copper. The chemical composition across the as-prepared copper phyllosilicate was addressed by EDX. Spot analysis of 22 regions of 100−1 μm in diameter revealed a Cu/Si atomic ratio of 0.59 with a standard deviation of 0.09, and 6 EDX line-scans of 100−500 nm in length, crossing several single platelets, revealed a Cu/Si ratio between 0.50 and 0.75 for all points (Figure S1−S3). Thus, the copper loading was very homogeneous throughout the as-prepared copper phyllosilicate with a composition of Cu/Si that agrees with the nominal ratio of 0.66.

Reduction of Copper Phyllosilicate. First, the reduction of copper phyllosilicate was addressed with TPR and TGA (Figure 2D). In TPR, the hydrogen consumption started at 220 °C, peaked at 255 °C and ceased above 270 °C. The amount of hydrogen consumed by this reduction was 140 cm^3 (STP)/g. The weight loss during the reduction up to 500 °C amounted to 15%, as determined by TGA. A minimum weight loss of 9% was expected based upon the loss of oxygen atoms acting as counterions for the Cu^{2+}. The additional 6% is presumably due to crystal water in the copper phyllosilicate. Taking into account the weight loss during reduction, the amount of H_2 consumed corresponded to the reduction of 40 wt % Cu^{2+} to Cu^0. Since the intended copper loading was ca. 41 wt %, it is concluded that copper phyllosilicate was fully reduced to metallic copper between 220 and 270 °C.[7d,9] Consistently, XRD showed the presence of crystalline metallic Cu and silica after reduction at 250 °C in a plug-flow reactor with 20% H_2 in Ar for 2.5 h (Figure 2A, red).

Next, the reduction was examined in the electron microscope by exposing the copper phyllosilicate to 1 mbar H_2 at different temperatures. Figure 3 shows TEM images of four different samples acquired after reduction for 4 h at 150 °C (A), and for 30 min at 200 °C (B), 250 °C (C) and 280 °C (D). That is, the TEM images show sample regions that were unexposed to the electron beam prior to and during the reduction. Therefore, the images show the results of transformations of the copper phyllosilicate that were inherent to the reduction process in the electron microscope, excluding any electron-beam-induced changes. The copper phyllosilicate appeared unchanged after reduction at 150 and 200 °C, in line with TGA and TPR. After 30 min at 250 °C, nanometer-sized particles were clearly visible as darker features on the brighter support. The average size of the nanoparticles was about 5 nm. Reducing the sample for up to 2 h resulted in the appearance of more nanoparticles and a further growth of the nanoparticles to an average size of 8 nm (not shown in Figure 3). At the higher temperature of 280 °C, the nanoparticles developed with an average size of 8 nm already after half an hour of reduction (Figure 3D). Extending
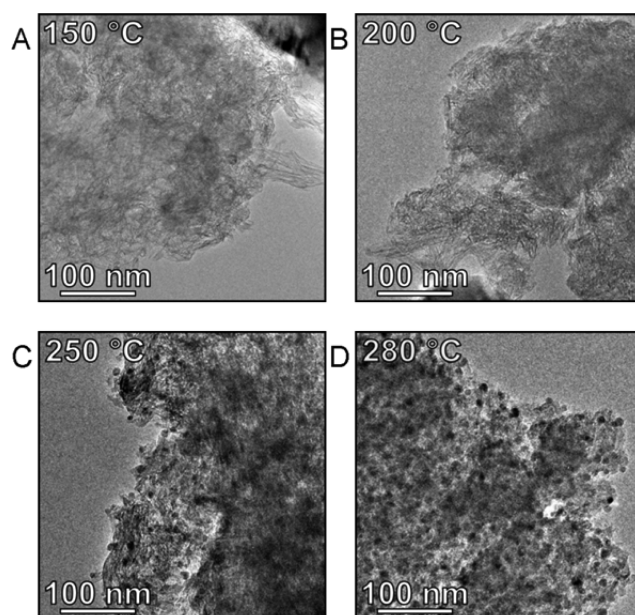

Figure 3. TEM images of copper phyllosilicate after exposure to 1 mbar H_2 at different temperatures and reaction conditions in the electron microscope. Reduction conditions: (A) 150 °C, 4 h (B) 200 °C, 30 min (C) 250 °C, 30 min and (D) 280 °C, 30 min. TEM image acquisition (A, B) in situ at 1 mbar H_2 at 150 °C and (C, D) at vacuum at room temperature.

the reduction treatment to longer reduction times and increasing the temperature to 310 °C (75 min at 280 °C and 30 min at 310 °C) did not lead to any further changes. Thus, the copper phyllosilicate was fully reduced to Cu/SiO_2 within 30 min at 280 °C in the electron microscope. Subsequently, the reduction in the electron microscope was compared to the reduction in a plug-flow reactor. For the latter sample, STEM-EDX spectra show similar Cu/Si atomic ratios as before reduction (Figure S4) and HR-TEM images reveal lattice fringes for the darker features with a spacing of ca. 2.09 Å, which corresponds to the distance between (111) planes in metallic copper (Figure S5). Figure 4 shows TEM images of the copper phyllosilicate and corresponding particle size distributions after reduction in the plug-flow reactor and in the electron microscope. The distributions, average particle size and standard deviation are similar (Table S2). Therefore, the formation of copper nanoparticles during reduction by H_2 in the microscope was representative for the formation process in a standard plug-flow reactor. Moreover, the comparison demonstrates that the particle formation was insensitive to the different H_2 pressure and heating rate employed in the two instruments.

Monitoring Nanoparticle Formation by TEM. During reduction in H_2, the copper phyllosilicate was monitored by TEM following the experimental scheme outlined in Figure 1. This scheme excludes electron illumination of the sample in the microscope's base vacuum prior to the reduction process, uses a low electron dose-rate, and fragments the accumulated electron dose to suppress the impact of the electron beam on the reduction process. The reduction was conducted at 280 °C, because that temperature is sufficiently high to complete the reduction while limiting the accumulated electron illumination time, and because it is still sufficiently low to allow for a good temporal resolution during the process of particle formation. Two separate experiments were conducted in which time-
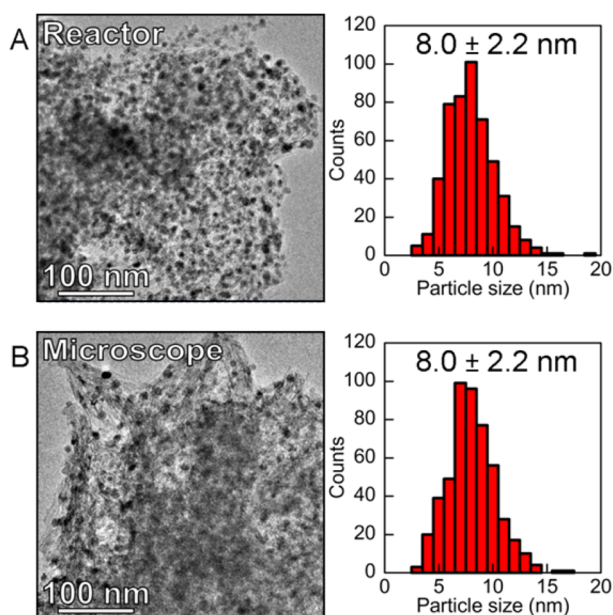
Figure 4. TEM images of copper phyllosilicate after reduction in a plug-flow reactor and in the electron microscope. (A) Copper phyllosilicate reduced in a plug-flow reactor (20% H_2 in Ar, 250 °C, 150 min) and rereduced in the electron microscope (1 mbar H_2, 250 °C, 45 min). The TEM image was acquired in situ at 1 mbar H_2 at 250 °C. The PSD is based on such TEM images of 17 different regions of the samples. (B) Copper phyllosilicate reduced in the electron microscope (1 mbar H_2, 280 °C, 30 min). The TEM image was acquired in vacuum at room temperature. The PSD is based on such images of 17 different regions. Each PSD includes the size of 500 copper nanoparticles and the number-averaged particle size and standard deviation of the distributions are included.

lapsed TEM image series were acquired of three distinct regions. In the first experiment, Region 1 was continuously illuminated during reduction. In the second experiment, Region 2 and Region 3 were intermittently illuminated with different time intervals (~2 and ~6 min) to address the effect of electron dose accumulation on the growth of copper nanoparticles. At the timed instants (Figure 1), TEM images were recorded enabling time-lapsed image series of the three regions during the reduction process. When such image series are played back as a movie, a vivid impression of the growth scenario is obtained. The movie of Region 1 is provided as Supporting Information (Movie S1). Figure 5 shows selected TEM images from the time-lapsed series of all three regions. After the reduction treatment, the sample was cooled to room temperature, and the electron microscope was evacuated to reestablish a base vacuum of 1.9×10^{-6} mbar. Under these conditions, TEM images were acquired of the three regions and of reference regions, which had not previously been illuminated by the electron beam.

The TEM images in Figure 5 reveal that the first appearance of copper nanoparticles occurred within the first few minutes at the reduction conditions. Because of the finite image SNR and resolution, it is possible that the particles had nucleated at earlier times and subsequently had grown beyond the size of 3 nm which is detectable in the TEM images. That is, the particle size at the first observation by TEM is likely larger than the critical size associated with the copper nanoparticle formation. Once formed, the nanoparticles remained immobile. This finding suggests that the continued growth (Figure 5) cannot

be a result of particle migration and coalescence under the present conditions.[12] Instead, the observations suggest that the nanoparticles grew by the attachment of smaller copper species, which are formed during the reduction treatment and which are sufficiently mobile to reach the nanoparticles. As the copper nanoparticles appear to have formed homogeneously across the precursor material, this mobility was probably limited to diffusion distances on the order of the final spacing between the nanoparticles, which is roughly 10 nm. Moreover, a close-up inspection of particles near the precursor agglomerate edge did not indicate any marked preference for specific nucleation sites.[7e] Thus, these observations suggest that the copper nanoparticles tended to nucleate homogeneously and grew by attachment of copper species from their vicinity.

To develop a kinetic description of these dynamic observations, the role of the actual electron illumination, which is shown in Figure 1, is addressed. This assessment is done by comparison of the particle evolution and final PSD of the three regions (Region 1, 2 and 3) to each other and by comparison of the final PSDs of the three regions to the PSD of reference regions (Figure 5). The PSDs of the three regions (Region 1, 2 and 3) were visually similar and their deviations were within the statistical error ($p_{\text{(same mean size)}} > 0.025$, Table S4). Thus, the accumulated electron dose used in the present experiment did not affect the final nanoparticle size. The PSDs of the three regions (Region 1, 2 and 3) were also visually and statistically similar to the reference regions, (Figure 5D) indicating that the applied illumination scheme was also of insignificant importance for the final nanoparticle size. Moreover, the stage of particle evolution was evaluated by tracking 25 visually distinguishable particles per region. Figure 6 shows the stage of particle evolution as a function of time for the three regions. Since only particles that were clearly visible throughout the experiment were measured, this analysis was biased toward larger particles resulting in a final average particle size close to 10 nm, instead of 8 nm (Figure 5). The progress of particle formation for the three regions (Region 1, 2 and 3) was close to identical, despite the different electron doses. Specifically, region 3 was imaged for the first time after 7 min at 1 mbar H_2 and 280 °C and the particle formation had progressed to the same extent as for Region 1, which had been continuously illuminated. This indicates that the electron illumination during reduction did not have a measurable influence on the evolution of the sample.

Quantitative information is obtained from measuring the sizes of the 25 individual particles in region 1 at different stages of the reduction, as shown in Figure 7 (black dots, see Figure S12 for corresponding particles). At the time for first appearance, all particles were larger than 3.4 nm. Most particles were detected after 2 to 6 min and all particles had appeared within 15 min. After its appearance, a particle grew initially fast and later slower until it had reached its final size within the following 10 min.

Kinetic Models for the Nanoparticle Formation. The TEM observations made in situ of nanoparticle formation provide information about the time for the first observation of a nanoparticle and about its subsequent growth. This dynamic information is hereafter compared with two kinetic models that are consistent with the observed dynamic behavior of the nanoparticles. For both models, it is assumed that the reduction process starts as the temperature reached 280 °C, because particle formation did not occur below 250 °C in the experiments and because the heating rate is fast (30 °C/min)
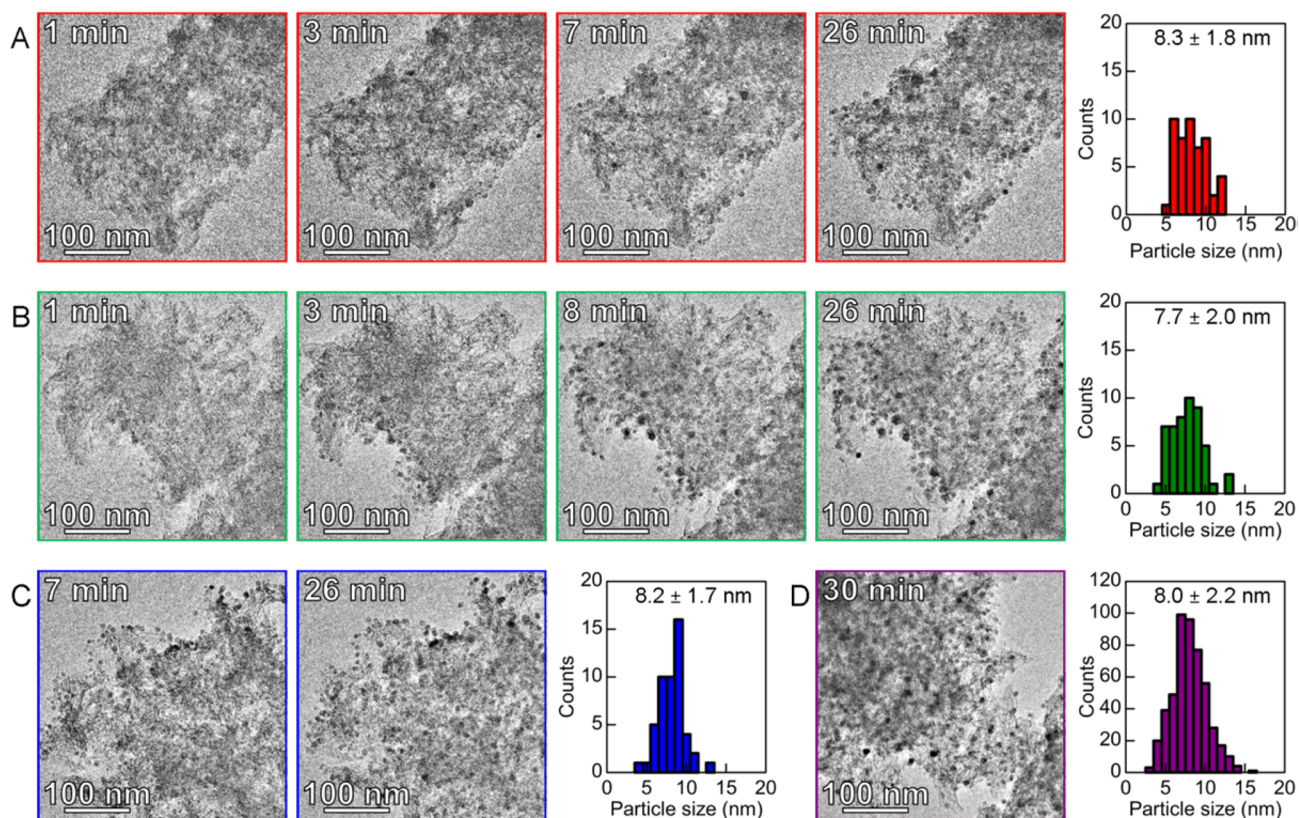
Figure 5. Time-resolved TEM images of copper phyllosilicate during exposure to 1 mbar H_2 at 280 °C. (A) Region 1 observed by continuous electron illumination at an electron dose-rate of 1 e⁻/(Å² s) (Supplementary Movie S1), and the corresponding PSD after reduction. (B) Region 2 observed with intermittent electron illumination at ca. 2 min intervals at an electron dose-rate of 1 e⁻/(Å² s) and the corresponding PSD after reduction. (C) Region 3 observed with intermittent electron illumination at ca. 6 min intervals at an electron dose-rate of 1 e⁻/(Å² s) and the corresponding PSD after reduction. (D) A TEM image of a reference region imaged after reduction and the PSD corresponding to 17 reference regions imaged after reduction. The PSDs include the number-averaged particle size and corresponding standard deviation.
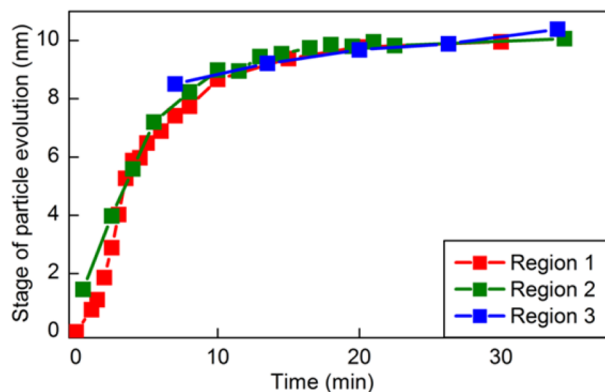

Figure 6. Stage of copper particle evolution versus time for reduction of copper phyllosilicate in 1 mbar H_2 at 280 °C. The stage of particle evolution is obtained from the time-resolved TEM images of Region 1−3 (Figure 5).

(Figure 3). Furthermore, variations in temperature over time or over different locations are considered negligible because the particle size evolved similarly in different areas (Figures 5, 6).

Nucleation-and-Growth Model. The first model considers the reduction of the phyllosilicate as a first order and irreversible reaction that feeds reduced mobile copper species to a reservoir and leads to a classical nucleation-and-growth scenario (e.g., DeBenedetti,[13] LaMer and Dinegar,[14] see Supporting Information). That is, as the concentration of

reduced species exceeds the saturation concentration, copper nuclei larger than a critical size are formed and subsequently grow by addition of diffusing reduced species. The concentration of these mobile reduced species is assumed to be uniform throughout the system, except for a diffusive boundary layer surrounding each particle (a mean-field approximation). As nucleation in this model is a statistical event, the model is consistent with a homogeneous distribution of nanoparticles. In the model, the size evolution of all particles was fitted with only two adjustable parameters, namely the kinetic constant of the reduction and the diffusion coefficient of the reduced species (see Supporting Information). The best fit of the model to the data in Figure 7 was obtained with a kinetic constant of 0.64 min⁻¹ and a diffusion coefficient of $\sim 5 \times 10^{-19}$ m²/s. With these parameters the model accounts reasonably for the observed nucleation times as well as for the growth of the nanoparticle size (see Figure 7, green lines and Figure S14).

However, the model has some implications that are physically improbable. Because nucleation does not occur until after a few minutes in the reduction treatment, a large fraction of the copper atoms must be present as mobile reduced copper species in the early phase (Figure S13). The peak amount of mobile reduced copper species exceeds 20% of all copper present, corresponding to a surface concentration of ~ 15 Cu atoms/nm² or about 100% of a monolayer. Such a high surface concentration is physically unrealistic. Another inconsistency of the model results from the mean-field approximation, which imposes that the chemical environment
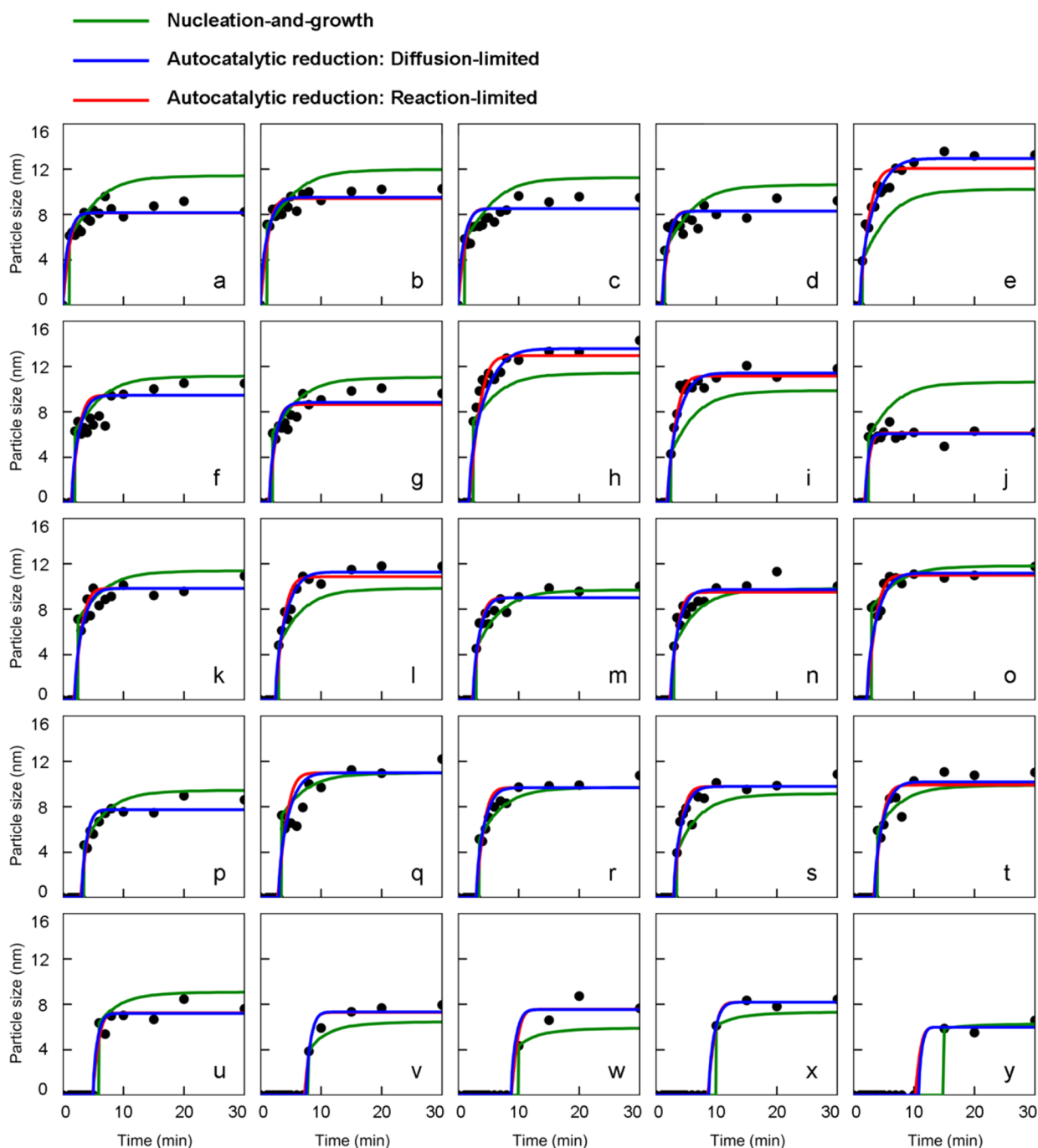
Figure 7. Size evolutions of the 25 copper particles selected in Region 1. The measured particle size is shown as black dots, the fitted nucleation-and-growth model is shown in green and the fitted autocatalytic model is shown in red (reaction-limited) and in blue (diffusion-limited).

of all nanoparticles is the same at any given time. As a consequence the final size of the particles should depend only on the nucleation time, which is contradicted by the data that exhibit a considerable scatter in the relation between nucleation time and final particle size (Figure 8). At last, it is expected that the reduction rate is sensitive to the H_2 pressure while the diffusion of reduced copper species is not. Since in the nucleation-and-growth model the ratio between the reduction rate and the diffusion coefficient determines the final particle size and density, the model predicts a higher particle density and smaller particle sizes at higher H_2 pressures. However, this prediction is inconsistent with the experimental observation

that the final particle size is insensitive to the H_2 pressure at 1 mbar and 200 mbar.

Autocatalytic Model. In the light of the high and homogeneous particle density (Figure 5) and the inability of the mean-field approximation to explain the scatter in the relation between nucleation time and final particle size, it seems inconsistent that a nanoparticle grew from mobile species originating from a distance far away. Rather, a nanoparticle is considered to capture species from a limited spatial zone of a few (tens of) nanometers in its vicinity. Therefore, the second model includes the additional assumption that the copper phyllosilicate is made up of regions, referred to as boxes, which do not exchange copper species. The structural characterization
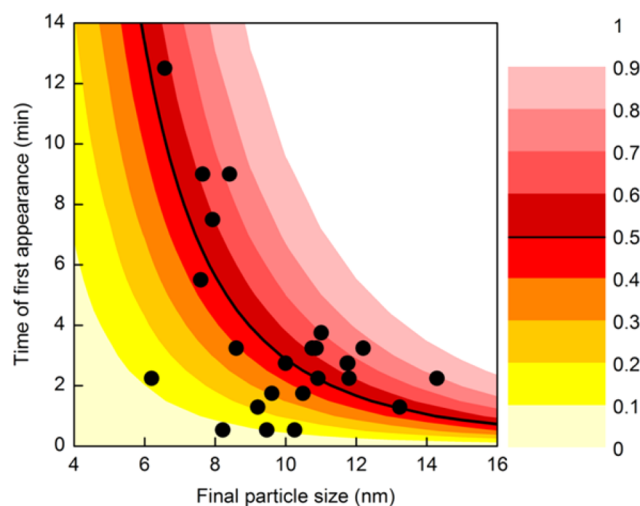
Figure 8. Observed time of first appearance of a particle against the observed final particle size (black dots). The colored regions indicate the cumulative probability according to Poisson statistics for nucleation to occur at a specific time for a given box size. Box sizes are expressed as the corresponding final particle sizes to aid the comparison with the observed experimental data.

of the copper phyllosilicate shows that the material consisted of agglomerations of platelets in the range of 5−20 nm in width and thickness and up to 100 nm in length (Figure 2). Logically, diffusion of copper species within a platelet is easier than from one platelet to another. It is thus probable that the copper particles effectively only grew from the copper phyllosilicate present in a certain volume. The final size of a particle is therefore related to the size of its surrounding copper phyllosilicate box. For example, an 8 nm copper particle would contain as many copper atoms as a copper phyllosilicate cubic box of size 17 nm. Depending on the exact dimensions of a copper phyllosilicate platelet this means that the phase transformation resulted into one or a few copper particles per platelet, which was also observed experimentally.[7e]

Since the appearance of particles seemed to be randomly occurring throughout the agglomerate and specific nucleation sites seemed to be absent, homogeneous nucleation was considered. In that light, every copper ion in a box is assumed to have a given probability of being reduced per unit of time and result in a particle nucleus. As shown in the Supporting Information, such a nucleation phenomenon is governed by Poisson statistics. As a consequence, the probability of early nucleation is higher in larger boxes corresponding to larger final particle sizes, which is in qualitative agreement with Figure 7. The reduction probability obtained from a maximum-likelihood analysis of the data is 5.42×10^{-6} min^{-1} ion^{-1} (see Supporting Information). Based on that probability and on an estimate of the corresponding box volume, obtained from the final particle size, the overall nucleation probabilities were calculated as a function of time and are shown in Figure 8. Most of the particles have a probability between 0.1 and 0.9 of having nucleated at the observed time. It has to be stressed that the Poisson model captures both the relation between the final size and the nucleation time, and the scatter in the data resulting from the inherently statistical nature of the process. The model assumes that only one particle nucleates in each box and that no secondary nucleation takes place. However, for large boxes corresponding to final particle sizes of about 13 nm, secondary nucleation should occur with a probability as large as 90% (see

Supporting Information). Secondary nuclei are therefore assumed to coalesce with the primary particle. Although no mobility of particles larger than 3.4 nm was observed, diffusion and coalescence of much smaller particles consisting of one or a few copper atoms can be expected to be fast.[12]

It is particularly interesting to observe that the statistical reduction rate of each ion before nucleation (5.42×10^{-6} min^{-1}) is orders of magnitude lower than the overall reduction rate, which is of the order of 0.64 min^{-1} according to the kinetic constant of the nucleation-and-growth model. This difference suggests that an autocatalytic process may be at play, in which the reduction is catalyzed by the newly formed copper particles. Autocatalytic reduction is often observed in the synthesis of supported metal catalysts,[2,15] and it has been shown that the reduction of CuO is autocatalytic.[16]

To model the growth of the nucleated particles, it is therefore assumed that the autocatalytic process starts as soon as a particle nucleus has been formed. In principle, particle growth during autocatalytic reduction could be either diffusion-limited or reaction-limited.[17] Both limiting cases were therefore considered in models fitted to the data. In the reaction-limited model (red lines in Figure 7, autocatalytic model$_{\text{reaction-limited}}$), the reduction and hence growth of the particles is assumed to be catalyzed by the copper surface and therefore proportional to the average Cu^{2+} concentration in the box.[15] The best fit of the model was obtained with a kinetic constant of ~0.45 nm/min, which corresponds to about 2 atomic layers per min. In the diffusion-limited model (blue lines in Figure 7, autocatalytic model$_{\text{diffusion-limited}}$), the reduction rate is high and all of the copper ions are considered to have the same mobility. The diffusion coefficient derived from fitting the model to the experimental data is 4.5×10^{-19} m^2/s, which is typical for solid state diffusion.[18] Extrapolated to 280 °C, coefficients around 1×10^{-16} m^2/s have been found for the diffusion of Cu$^+$ ions in sodium enriched silica.[19] Gonella et al. have reported that the diffusion of Cu^{2+} is about 2 orders of magnitude slower than that of Cu$^+$.[20]

The experimental results are well described by both the diffusion-limited and the reaction-limited model and do not allow to distinguish between the two. In conclusion, the autocatalytic model seems to better describe all of the observations in Figure 5 compared to the nucleation-and-growth model. Therefore, the autocatalytic model is a more attractive model for describing the reduction mechanism. It is plausible that initial particle growth is reaction-limited since the surrounding area is not yet depleted of copper. Analogous to this, the final stage of particle growth is more likely to be diffusion-limited since at that time the surrounding area is depleted of copper. Thus, a combination of the two limiting autocatalytic models could be possible for describing the observations.

■ CONCLUSION

In situ TEM was used to examine the phase transformation of homogeneous copper phyllosilicate platelets, a prototype precursor for a coprecipitated catalyst, during its reduction in hydrogen resulting in the formation of copper nanoparticles on a silica support. Similar particle size distributions after reduction in the electron microscope and in a plug-flow reactor were obtained, validating that the phase transformation inside the microscope was representative for the phase transformation in a plug-flow reactor. On the basis of an assessment of the electron beam illumination prior to and during reduction, a procedure

was developed for time-resolved imaging of the dynamical changes of the copper phyllosilicate that are inherent to the reduction process. After an induction time of a few minutes, particles with a size larger than 3.4 nm were detected throughout the sample and grew in about 10 min to their final size of about 8 nm. Particle mobility was not observed indicating that growth of particles larger than 3.4 nm occurred via the diffusion of mobile copper species (likely Cu^{2+} ions) and their attachment to the copper particles. The size evolution of the particles was measured and was well described by a two-step reduction mechanism with either diffusion-limited or reaction-limited particle growth. It is concluded that reduction of copper phyllosilicate in H_2 to silica supported copper particles is autocatalytic and occurs via the diffusion of copper species. The plate-like structure of the precursor restricted the diffusion of copper and the autocatalytic reduction limited the probability for secondary nucleation. The combination of a uniform size of precursor particles and the autocatalytic reduction thus offers means to synthesize nanoparticles with well-defined sizes in large amounts. Hence, with careful optimization of the imaging strategy, time-resolved TEM provided unique mechanistic and kinetic information about the nucleation and growth of nanoparticles that is representative for large-scale nanomaterial synthesis.

■ ASSOCIATED CONTENT

Ⓢ Supporting Information

The Supporting Information is available free of charge on the ACS Publications website at DOI: 10.1021/jacs.5b12800.

> Figures S1−S18, Tables S1−S4, and a description of the kinetic models. (PDF)
> Movie with time-lapsed TEM images during reduction at 280 °C at 1 mbar H_2 of Region 1. (AVI)

■ AUTHOR INFORMATION

Corresponding Author
*E-mail: sth@topsoe.dk.
Notes
The authors declare no competing financial interest.

■ ACKNOWLEDGMENTS

■ REFERENCES

(1) (a) Schüth, F.; Hesse, M.; Unger, K. K. Precipitation and coprecipitation. In *Handbook of Heterogeneous Catalysis*; Ertl, G., Knözinger, H., Schüth, F., Weitkamp, J., Eds.; Wiley-VCH Verlag GmbH & Co. KGaA: Weinheim, 2008. (b) Behrens, M. *Catal. Today* **2015**, *246*, 46−54. (c) de Jong, K. P., Ed.; *Synthesis of Solid Catalysts*; Wiley-VCH: Weinheim, 2009. (d) Yin, Y.; Alivisatos, A. P. *Nature* **2005**, *437*, 664−670. (e) Peng, Z.; Kisielowski, C.; Bell, A. T. *Chem. Commun.* **2012**, *48*, 1854−1856.

(2) Mondloch, J. E.; Bayram, E.; Finke, R. G. *J. Mol. Catal. A: Chem.* **2012**, *355*, 1−38.

(3) (a) Gontard, L. C.; Chang, L. Y.; Hetherington, C. J.; Kirkland, A. I.; Ozkaya, D.; Dunin-Borkowski, R. E. *Angew. Chem., Int. Ed.* **2007**, *46*, 3683−3685. (b) Zhu, Y.; Ramasse, Q. M.; Brorson, M.; Moses, P. G.; Hansen, L. P.; Kisielowski, C. F.; Helveg, S. *Angew. Chem., Int. Ed.* **2014**, *53*, 10723−10727.

(4) (a) Boyes, E. D.; Gai, P. L. *Ultramicroscopy* **1997**, *67*, 219−232. (b) Sharma, R.; Crozier, P. A. Environmental transmission electron microscopy in nanotechnology. In *Handbook of Microscopy for Nanotechnology*; Yao, N., Wang, Z. L., Eds.; Kluwer Academic Publishers: New York, 2005; pp 531−565. (c) Hansen, P. L.; Helveg, S.; Datye, A. K. *Adv. Catal.* **2006**, *50*, 77−95. (d) Creemer, J. F.; Helveg, S.; Hoveling, G. H.; Ullmann, S.; Molenbroek, A. M.; Sarro, P. M.; Zandbergen, H. W. *Ultramicroscopy* **2008**, *108*, 993−8. (e) de Jonge, N.; Ross, F. M. *Nat. Nanotechnol.* **2011**, *6*, 695−704.

(5) (a) Woehl, T. J.; Evans, J. E.; Arslan, I.; Ristenpart, W. D.; Browning, N. D. *ACS Nano* **2012**, *6*, 8599−8610. (b) Liao, H. G.; Zheng, H. *J. Am. Chem. Soc.* **2013**, *135*, 5038−5043. (c) Williamson, M. J.; Tromp, R. M.; Vereecken, P. M.; Hull, R.; Ross, F. M. *Nat. Mater.* **2013**, *2*, 532−536.

(6) (a) Banerjee, R.; Crozier, P. A. *J. Phys. Chem. C* **2012**, *116*, 11486−11495. (b) Li, P.; Liu, J.; Nag, N.; Crozier, P. *Appl. Catal., A* **2006**, *307*, 212−221. (c) Li, P.; Liu, J.; Nag, N.; Crozier, P. A. *Surf. Sci.* **2006**, *600*, 693−702. (d) Hayden, T. F.; Dumesic, J. A.; Sherwood, R. D.; Baker, R. T. K. *J. Catal.* **1987**, *105*, 299−318. (e) Li, P.; Liu, J.; Nag, N.; Crozier, P. A. *J. Catal.* **2009**, *262*, 73−82. (f) Hansen, L. P.; Johnson, E.; Brorson, M.; Helveg, S. *J. Phys. Chem. C* **2014**, *118*, 22768−22773. (g) Li, P.; Liu, J.; Nag, N.; Crozier, P. A. *J. Phys. Chem. B* **2005**, *109*, 13883−13890.

(7) (a) Zhu, S.; Gao, X.; Zhu, Y.; Fan, W.; Wang, J.; Li, Y. *Catal. Sci. Technol.* **2015**, *5*, 1169−1180. (b) Simonov, M. N.; Zaikin, P. A.; Simakova, I. L. *Appl. Catal., B* **2012**, *119−120*, 340−347. (c) Gong, J.; Yue, H.; Zhao, Y.; Zhao, S.; Zhao, L.; Lv, J.; Wang, S.; Ma, X. *J. Am. Chem. Soc.* **2012**, *134*, 13922−13925. (d) Chen, L.; Guo, P.; Qiao, M.; Yan, S.; Li, H.; Shen, W.; Xu, H.; Fan, K. *J. Catal.* **2008**, *257*, 172−180. (e) van den Berg, R.; Zečević, J.; Sehested, J.; Helveg, S.; de Jongh, P. E.; de Jong, K. P. *Catal. Today* **2015**, DOI: 10.1016/j.cattod.2015.08.052. (f) Behrens, M.; Studt, F.; Kasatkin, I.; Kuhl, S.; Havecker, M.; Abild-Pedersen, F.; Zander, S.; Girgsdies, F.; Kurr, P.; Kniep, B. L.; Tovar, M.; Fischer, R. W.; Nørskov, J. K.; Schlögl, R. *Science* **2012**, *336*, 893−897. (g) Hansen, J. B.; Hojlund Nielsen, P. E. Methanol Synthesis. In *Handbook of Heterogeneous Catalysis*; Ertl, G., Knozinger, H., Schuth, F., Weltkamp, J., Eds.; Wiley-VCH, 2008; pp 2920−2949.

(8) (a) Toupance, T.; Kermarec, M.; Lambert, J.-F.; Louis, C. *J. Phys. Chem. B* **2002**, *106*, 2277−2286. (b) van der Grift, C. J. G.; Elberse, P. A.; Mulder, A.; Geus, J. W. *Appl. Catal.* **1990**, *59*, 275−289.

(9) Huang, Z.; Cui, F.; Xue, J.; Zuo, J.; Chen, J.; Xia, C. *J. Phys. Chem. C* **2010**, *114*, 16104−16113.

(10) Jinschek, J. R.; Helveg, S. *Micron* **2012**, *43*, 1156−1168.

(11) ANOVA analysis performed using Analysis ToolPak in Excel 2010.

(12) Wynblatt, P.; Gjostein, N. A. *Prog. Solid State Chem.* **1976**, *9*, 21−58.

(13) Debenedetti, P. G. *Metastable Liquids: Concepts and Principles*; Princeton University Press: Princeton, NJ, 1996.

(14) LaMer, V. K.; Dinegar, R. H. *J. Am. Chem. Soc.* **1950**, *72*, 4847−4854.

(15) Watzky, M. A.; Finke, R. G. *J. Am. Chem. Soc.* **1997**, *119*, 10382−10400.

(16) (a) Tiernan, M. J.; Barnes, P. A.; Parkes, G. M. B. *J. Phys. Chem. B* **1999**, *103*, 338−345. (b) Pease, R. N.; Taylor, H. S. *J. Am. Chem. Soc.* **1921**, *43*, 2179−2188.

(17) Aiken, J. D.; Finke, R. G. *J. Am. Chem. Soc.* **1998**, *120*, 9545−9554.

(18) Heitjans, P.; Kärger, J. *Diffusion in Condensed Matter*; Springer-Verlag: Berlin, 2005.

(19) Kaufmann, J.; Rüssel, C. *J. Non-Cryst. Solids* **2010**, *356*, 1158−1162.

(20) Gonella, F.; Quaranta, A.; Padovani, S.; Sada, C.; D'Acapito, F.; Maurizio, C.; Battaglin, G.; Cattaruzza, E. *Appl. Phys. A: Mater. Sci. Process.* **2005**, *81*, 1065−1071.